PHYSICS

Directly visualizing the momentum-forbidden dark excitons and their dynamics in atomically thin semiconductors

Julien Madéo[1]*, Michael K. L. Man[1]*, Chakradhar Sahoo[1,2], Marshall Campbell[3], Vivek Pareek[1], E. Laine Wong[1]†, Abdullah Al-Mahboob[1], Nicholas S. Chan[1], Arka Karmakar[1], Bala Murali Krishna Mariserla[1,4], Xiaoqin Li[3], Tony F. Heinz[5,6], Ting Cao[5,7], Keshav M. Dani[1]‡

Resolving momentum degrees of freedom of excitons, which are electron-hole pairs bound by the Coulomb attraction in a photoexcited semiconductor, has remained an elusive goal for decades. In atomically thin semiconductors, such a capability could probe the momentum-forbidden dark excitons, which critically affect proposed opto-electronic technologies but are not directly accessible using optical techniques. Here, we probed the momentum state of excitons in a tungsten diselenide monolayer by photoemitting their constituent electrons and resolving them in time, momentum, and energy. We obtained a direct visual of the momentum-forbidden dark excitons and studied their properties, including their near degeneracy with bright excitons and their formation pathways in the energy-momentum landscape. These dark excitons dominated the excited-state distribution, a surprising finding that highlights their importance in atomically thin semiconductors.

The discovery of two-dimensional (2D) semiconductors launched exciting opportunities in exploring excited-state physics and opto-electronic technologies (*1*–*3*), driven in part by the existence of robust, few-particle excitonic states. As a prototypical 2D semiconductor in the transition metal dichalcogenide (TMD) family, WSe_2 monolayers exhibit a band structure that hosts two degenerate valence band maxima but eight nearly degenerate conduction band minima in the hexagonal Brillouin zone (BZ) (*4*, *5*). At the K and K′ valleys, the conduction and valence band energies are both at local extrema, giving rise to two direct bandgap transitions and the bright excitons (denoted as K-K excitons) (Fig. 1, A and B). These excitons, also called direct excitons in the traditional semiconductor literature, are behind the strong light absorption and photoluminescence in the WSe_2 monolayer (*6*, *7*) and have been extensively investigated in various optical spectroscopy experiments.

Few experiments, however, have been capable of probing the indirect or momentum-forbidden dark excitons in monolayer TMDs, which consist of an electron and a hole residing at different valleys (*8*). Such dark excitons may interact with bright excitons, serve as the preferred carriers of information and energy, or form collective states such as exciton liquids and condensates (*9*, *10*). Therefore, determining the properties and controlling the population of the dark excitons, as well as their interactions with the bright excitons, is the key to a complete understanding of the underlying physics and developing future technologies. Because of the six other conduction band minima at the Q valleys (also denoted as Λ or Σ in the literature) in WSe_2 monolayers, dark excitons may form with an electron in the Q valley and a hole in the K (or K′) valley (Fig. 1A) (*5*, *11*). Compared with other TMDs, a near degeneracy between the Q- and K-valley states of WSe_2 has been predicted (*12*), furthering the possibility that these dark excitons play an important role in the optical properties (*13*). The crystal momentum mismatch between the electrons and holes makes them inaccessible in first-order optical processes such as absorption and photoluminescence (*14*, *15*).

Momentum-resolved studies of excitons have been a long-standing goal (*16*–*23*). Such studies would provide the resolution to directly access the recently sought-after dark excitons in monolayer TMDs (*14*, *24*). In general, angle-resolved photoemission spectroscopy (ARPES)–based techniques have been one of the most successful in providing momentum information (*25*). For example, ARPES techniques have successfully probed free carriers in bulk TMDs (*26*–*28*) and specially prepared monolayers (*30*–*32*). However, observing strongly bound, few-particle excitonic states is not straightforward even conceptually, as discussed in a number of recent theoretical studies (*19*–*23*). Experimentally, serious challenges include the need for high-energy extreme ultraviolet (XUV) photons to access states at the BZ vertices (XUV-ARPES), spatial resolution to study the typical high-quality micrometer-scale TMD samples (μ-ARPES) (*8*), and time resolution through a pump-probe configuration (TR-ARPES) to access the dynamics of the short-lived excitonic states after photoexcitation (*33*–*36*). Here, we successfully overcame these experimental challenges in a single platform to perform TR-XUV-μ-ARPES, providing a direct visualization of dark excitons in a WSe_2 monolayer. We report on dark exciton formation pathways under different photoexcitation conditions, the nature of their spectral degeneracy relative to bright excitons, and the dominant role they play in the quasi-equilibrium distribution at long time delays. Our experiments represent a milestone in studies of photoexcited states by providing a global view over the entire BZ, along with exclusive insights inaccessible otherwise.

We studied an exfoliated WSe_2 monolayer placed on an hBN buffer layer supported by an Si substrate (Fig. 1C). The sample was probed at a temperature of 90 K under ultrahigh vacuum conditions (details about sample preparation and characterization are provided in the supplementary materials). Our experiments are enabled by a custom-built platform that combines an ultrafast, tabletop XUV source with a spatially resolving photoemission electron microscope (PEEM) (Fig. 1D and supplementary text, section 2). First, we performed an XUV-μ-ARPES measurement to obtain the band structure of the nonphotoexcited WSe_2 monolayer (Fig. 2A). For this, we used ultrafast XUV probe pulses (21.7 eV) to photoemit electrons from the sample. Using the high-resolution spatial imaging capabilities of our PEEM apparatus, we isolated photoelectrons emitted from only the monolayer region of the sample (see the supplementary text, section 3). The reciprocal images of these photoelectrons were then dispersed in energy in a time-of-flight detector, thereby resolving the angle (i.e., momentum) and energy (with an energy resolution of 0.03 eV) of each photoelectron (*37*, *38*) (Fig. 1D and supplementary text, sections 2 to 4). The measured band structure showed the spin-split valence band extrema at the K,K′ valleys and had excellent agreement with GW calculations (Fig. 2A and materials and methods). The energy differences between the K- and Q-valley conduction bands were sensitive to the lattice parameters and functional used in the calculation (see the materials and methods).

Next, to measure the excitonic states of the TMD monolayer, we excited the sample with an ultrafast pump pulse tunable over the

[1]Femtosecond Spectroscopy Unit, Okinawa Institute of Science and Technology, Okinawa, Japan 904-0495. [2]School of Physics, University of Hyderabad, Gachibowli, Hyderabad-500046, Telangana, India. [3]Physics Department, Center for Complex Quantum System, The University of Texas at Austin, Austin, TX 78712, USA. [4]Department of Physics, Indian Institute of Technology, Jodhpur, Rajasthan, India 342037. [5]Department of Applied Physics, Stanford University, Stanford, CA 94305, USA. [6]SLAC National Accelerator Laboratory, Menlo Park, CA 94720, USA. [7]Department of Materials Sciences and Engineering, University of Washington, Seattle, WA 98195, USA.
*These authors contributed equally to this work.
†Present address: Center for Nano Science & Technology, Italian Institute of Technology, 20133 Milan, Italy.
‡Corresponding author. Email: KMDani@oist.jp

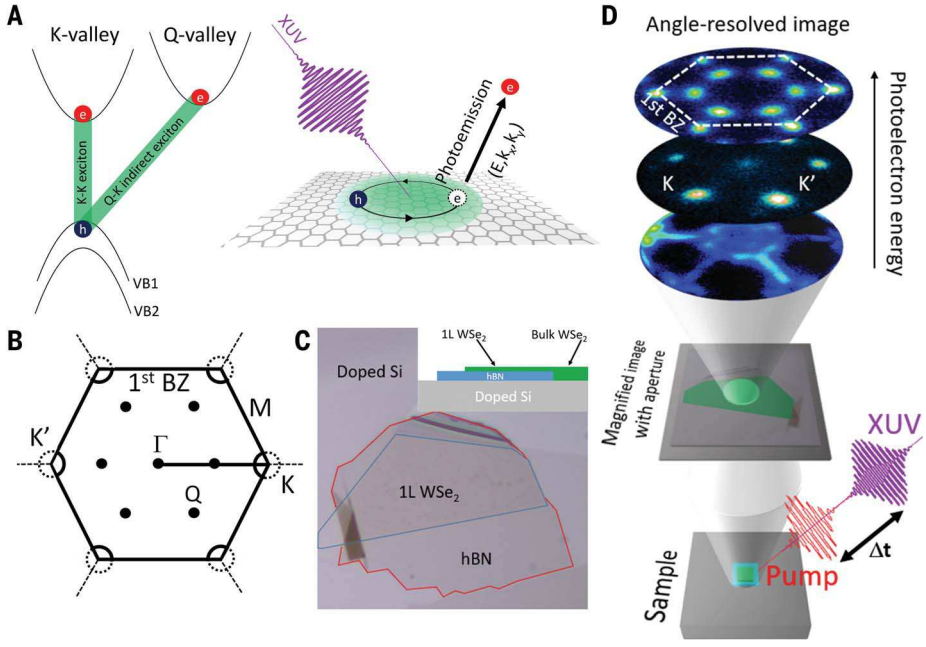

Fig. 1. Time-resolved-XUV-μ-ARPES of excitons in a WSe_2 monolayer. (**A**) Left: Diagram showing the configuration for K-K direct excitons and Q-K indirect excitons with holes located in the K valleys and electrons in K and Q valleys, respectively. Right: Representation of the exciton photoemission process. XUV photons photoemit electrons, leaving holes from the bound electron-hole pairs. (**B**) Schematic of the k-space structure of monolayer WSe_2 showing the first BZ composed of six Q valleys and two K valleys (each K valley is shared between three BZs, so only one-third of each falls within the first BZ). (**C**) Optical image of the sample composed of a monolayer WSe_2 (blue outline) on hBN (red outline) on an *n*-doped Si substrate. Inset is a side view of the sample. (**D**) Schematic of the experimental setup.

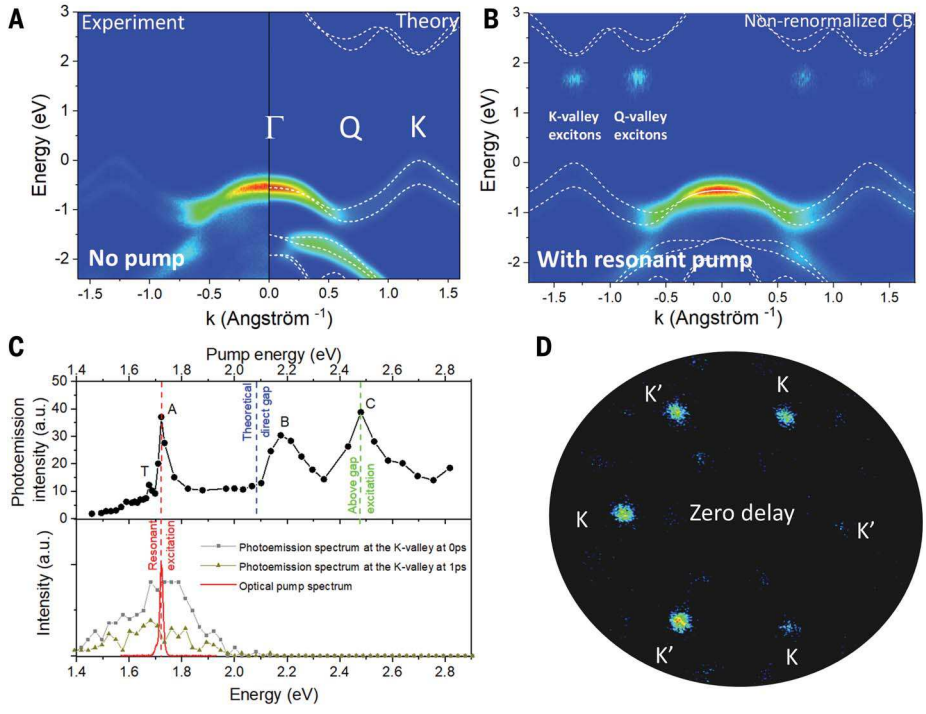

Fig. 2. Excitonic resonances. (**A**) Experimental and theoretical XUV-μ-ARPES results from the WSe_2 monolayer without optical excitation. The dispersion of the occupied quasiparticle bands (false color scale of electron emission intensity) is shown, together with the calculated band structure plotted along Γ-Q-K-M (dashed white lines). (**B**) Experimental band structure with a 1.72-eV photoexcitation resonant with the A exciton at a 0.5-ps delay showing below conduction band direct and indirect excitonic states. The experimental data were compared with nonrenormalized conduction bands with exciton-induced bandgap renormalization effects estimated to be <100 meV (*20*). (**C**) Top: Photoemission intensity integrated from 1 to 3 eV above the valence band maximum (VBM) versus optical pump energy. Seen clearly is the spectrum dominated by resonance at 1.73, 2.17, and 2.48 eV, corresponding to the A, B, and C excitons described in the literature, respectively. The observed resonance at low energy is attributed to the trion peak (*8*). Bottom: Spectrum of the resonant optical pump (red) and photoemission energy spectrum integrated within a ±0.015 $Å^{-1}$ k-space range at the center of the K valley at zero time delay (gray) and also at later time delays (green). (**D**) Corresponding momentum-resolved photoemission intensity integrated from 1 to 3 eV above the VBM showing the exciton signals in the K valley for a resonant excitation with the A exciton at zero time delay. The observed asymmetry in the intensity distribution is largely caused by the matrix element effect determined by the polarization and incidence angle of the photoemission probe.

visible and near-infrared range of the spectrum. Then, the ultrafast XUV probe pulse discussed above was introduced at a variable time delay to measure the time-, angle-, and energy-resolved photoelectron spectrum from the WSe_2 monolayer (TR-XUV-μ-ARPES). Recent theoretical studies have predicted photoemission signals from excitons exhibiting an energy-momentum distribution centered in the corresponding conduction band valley but binding energy below the conduction band minimum. In our measurements, after resonant photoexcitation of the A exciton, a substantial photoemission signal at positive time delay was seen below the bandgap centered at the K (K′), located at ±1.26 $Å^{-1}$, and Q valleys, located at ±0.75 $Å^{-1}$ (Fig. 2B) (*21*). To ensure that the detected signals corresponded to excitonic states, we measured the photoemission excitation spectrum (Fig. 2C, top panel), i.e., the integrated photoemission

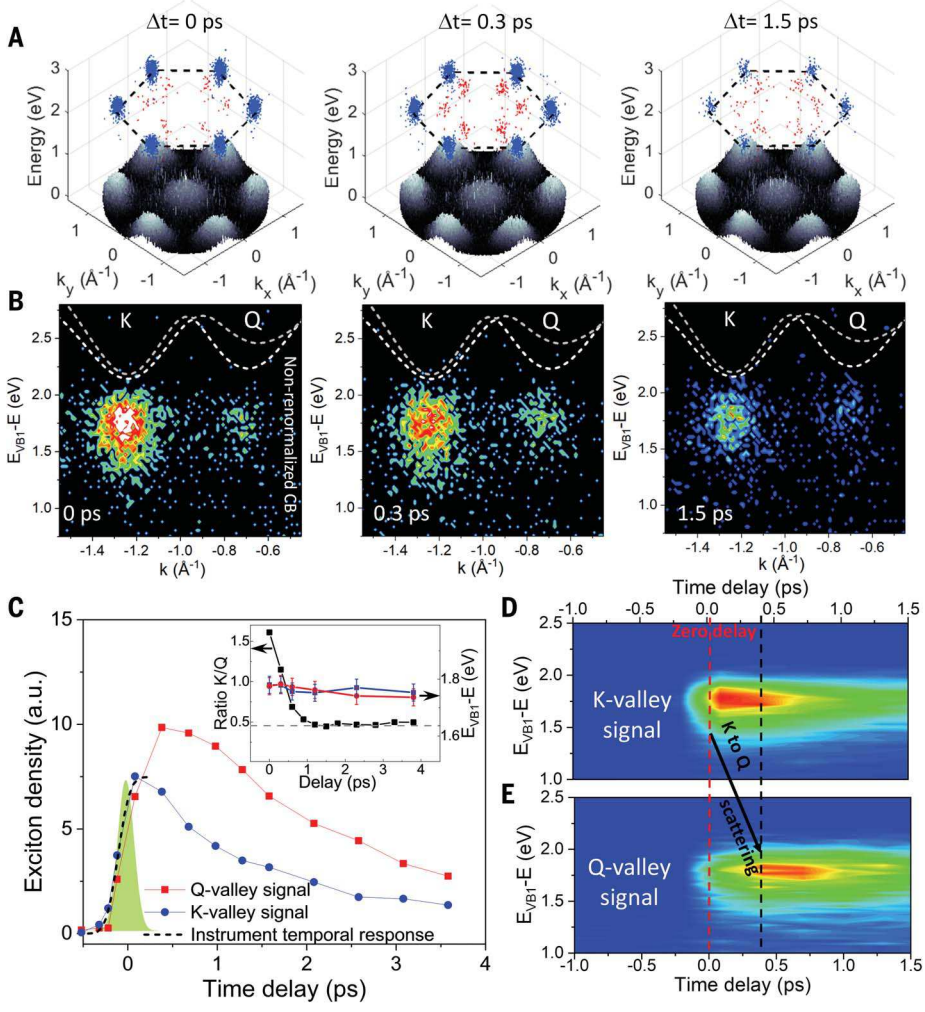

Fig. 3. Exciton dynamics after resonant excitation. (**A**) TR-ARPES data for delay times of 0, 0.3, and 1.5 ps for the full 2D BZ (in-plane) and emission energy (vertical). The top of the valence bands is displayed in grayscale; emission from the K-valley (Q-valley) excitons is plotted in blue (red) dots (see the supplementary materials). The black dashed line defines the boundary of the first BZ. (**B**) TR-ARPES data for delay times of 0, 0.3, and 1.5 ps along the line connecting the K and Q valleys. The dotted lines show the calculated (spin-split) conduction bands. (**C**) Exciton density versus time delay at Q valleys (red) and K valleys (blue). The exciton density was determined by the ARPES signal integrated over the two K valleys or six Q valleys of the first BZ and an energy range from 1 to 2.5 eV, with a correction factor for the respective photoemission matrix elements. The dotted black line shows the instrument response function, i.e., the convolution of the pump and probe pulse. The corresponding Gaussian pulse is plotted in green. Inset is the ratio of the K/Q population (black) obtained by dividing the data in Fig. 3C showing dominant K-valley exciton population initially but a ratio approaching ~0.5 at longer time delays. The blue and red curves correspond to the center energy of a Gaussian fit of the distributions of the K- and Q-valley signals, respectively. (**D**) Time-resolved spectrum of the K-valley signal integrated over the first BZ. (**E**) Time-resolved spectrum of the Q-valley signal integrated over the first BZ. K-valley excitons are populated directly upon photoexcitation. We observed a clear delay in the rise of the Q-valley population caused by K to Q scattering.

intensity (from 1 to 2.5 eV above VB1 in the first BZ), versus the optical excitation energy (varied from 1.58 to 2.85 eV). In the photoemission excitation spectrum, we clearly observed the distinctive A-, B-, and C-exciton resonances as previously reported in optical absorption (*6*). This energy dependence confirms the dominance of excitons under the experimental conditions used in this work, namely photoexcitation density, sample structure, and photoemission probe. Then, we tuned our pump pulse to 1.72 eV to match the A-exciton resonance as shown in the bottom panel of Fig. 2C. This choice of pump wavelength ensured that we were predominantly and resonantly exciting excitons. Finally, looking at the energy- and momentum-resolved photoemission signal under these pump conditions, we clearly saw a signal in the K valley and also at exactly the energy of the A exciton. This confirms that the photoemission signal at ~1.73 eV, located at ±1.26 $Å^{-1}$ along the K-Γ cut (i.e., in the K-valley), corresponds to excitons in the K valley, in agreement with previous theoretical calculations (*39*) and optical experiments (*40*). By extension, given the expected near degeneracy, we attribute the signal at 1.73 eV and ±0.75 $Å^{-1}$ momentum along the K-Γ cut to excitons in the Q valley. We assigned these two signals in part to the bright K-K and momentum-forbidden dark Q-K excitons, respectively (see the supplementary text, section 7). Given the large inhomogeneous broadening (~250 meV) in the photoemission spectrum of our sample (see the supplementary text, section 5), we expect that the K-valley signal also constitutes other excitonic states that are nearly resonant with the bright K-K exciton, such as the spin-dark K-K exciton, the indirect K-K′ exciton, as well as trions and biexcitons. Similar considerations also apply for the Q-valley signal. In the following, we will refer to the ensemble of excitonic states that constitutes the K- and Q-valley signals as K- and Q-valley excitons. We note that the calculated single-particle band structure in this work does not include renormalization effects caused by the exciton density, but we estimate this renormalization to be <100 meV (*20*). We also observed the K- and Q-valley excitons with electrons at the K,K′ and Q valleys and the presence of holes that could be seen by the depletion of electrons in the K,K′ valley by taking the difference between the band structures without and after photoexcitation (fig. S14A). The photoemission spectrum taken at different time delays (fig. S14B) after photoexcitation then allowed us to follow the formation dynamics of these dark indirect excitons and learn other aspects of their nature. To eliminate rigid energy shifts or offsets of the entire band structure caused by surface photovoltage effect or other similar phenomena, we set the peak of the upper spin-split valence band as the zero-energy reference for every time delay (see the supplementary text, section 8). We also used an optical excitation spot much larger than the sample to eliminate any lateral contribution to surface photovoltage caused by local variations of intensity (*41*).

To study the formation dynamics, we next resonantly excited the optically allowed K-K exciton as seen in Fig. 2C. We used linearly

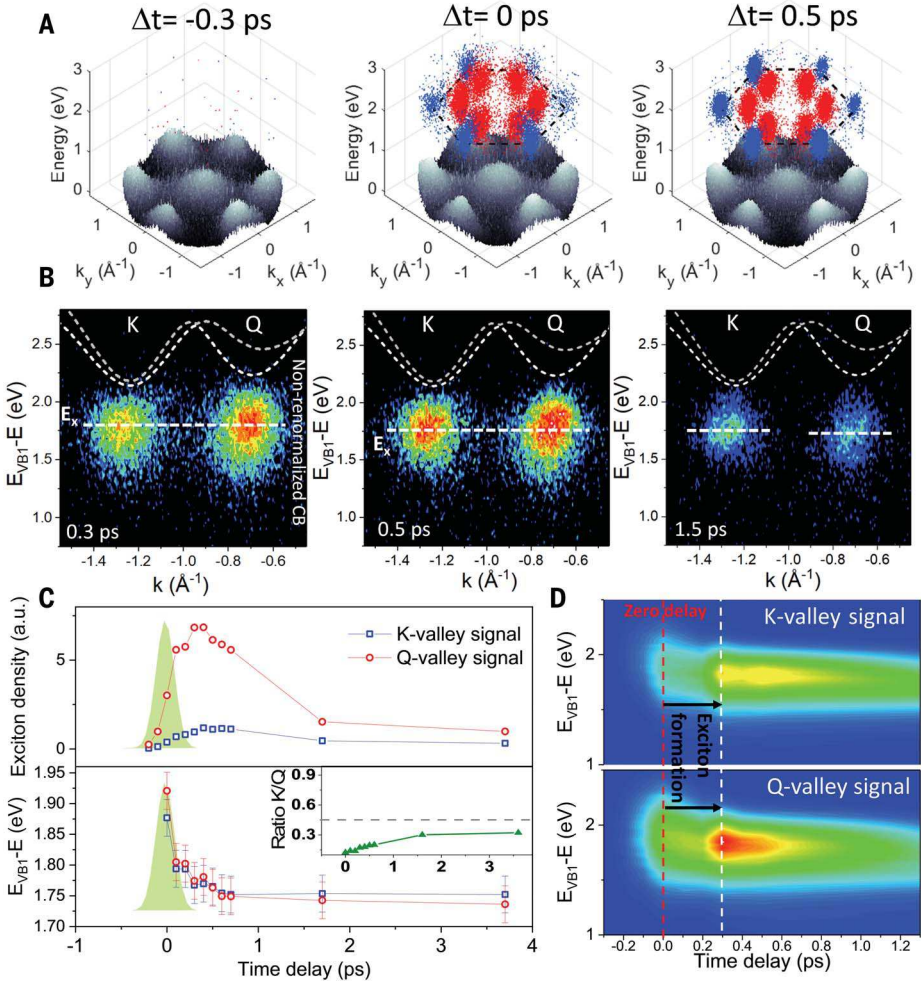

Fig. 4. Exciton formation and dynamics after above-gap excitation. (**A**) 3D plots of the experimental data at 0.3-, 0.5-, and 1.5-ps time delays. The top of the valence bands is displayed in grayscale. The K-valley (Q-valley) excitons are plotted in blue (red) dots. The black dashed line defines the boundary of the first BZ. (**B**) ARPES data at the K and Q valleys for 0.3-, 0.5-, and 1.5-ps time delays. Dotted line is the theoretical calculation of the conduction bands. (**C**) Top: K-valley (blue) and Q-valley (red) exciton density over the first BZ from 1 to 2 eV. Bottom: Center energy of the photoexcited population obtained from fits with Gaussian function at the center of the K and Q valley. Inset is the ratio of the total populations between the K and Q valleys extracted from the top panel. (**D**) Time-resolved spectra at the K valley (top) and the Q valley (bottom) showing the formation and relaxation of excitons.

polarized pump pulses at 1.72 eV with a fluence chosen to produce an estimated exciton density of 2.4 × 10^{12}/cm^2 (see the materials and methods and supplementary text, section 16). At zero-time delay, we observed only the K-valley excitons (Fig. 3, A and B). As expected for resonant excitation, the formation of K-valley excitons was rapid, as seen in Fig. 3C. The energy of the K-valley exciton (1.73 ± 0.03 eV) was consistent with the energy of the pump excitation, within experimental uncertainty, and did not change for longer delay times (Fig. 3C). At later times, we saw a clear buildup of the dark Q-valley exciton population at energies nearly degenerate (within our 0.03-eV energy resolution) with the K-valley excitons (Fig. 3D). Through the momentum sensitivity of the measurement, we directly observed the formation of the dark Q-valley excitons through scattering from the K-valley excitons on an ~400-fs time scale (see the supplementary text, section 13). Theoretical studies and indirect optical measurements have reported on phonon-assisted intervalley scattering of excitons (*23*, *42*–*44*) that are fundamentally different from the electron-phonon interactions seen in bulk TMDs (*28*). Our measurements directly accessed this exciton-phonon scattering and are consistent with the reported time scales of few hundred femtoseconds. Given the presence of resident carriers from unintentional doping, exciton-plasmon scattering could also play a role. Future experiments varying the doping concentration would allow one to tease out this contribution. The Q and K signals also showed similar recovery times, which is consistent with previous studies showing that the dark Q-K exciton acts as a long-lived reservoir for the K-K exciton (*45*). The extracted decay times were 1.7 and 2.5 ps for K- and Q-valley excitons, respectively (see the supplementary text, section 14), reflecting an average decay time corresponding to all the different excitonic states probed. Future experiments using samples with narrower linewidths in the ARPES signal could allow one to distinguish between the different excitonic states and the corresponding dynamics between them. Also of importance is the evolution to a quasi-equilibrium distribution of excitons. We initially created a larger K-valley population by resonant excitation with the A exciton, but within a picosecond, the Q-valley exciton population dominated, with the K-valley/Q-valley ratio tending toward ~0.5 (Fig. 3C, inset). We note that in calculating the ratio, we included the population in the entire first BZ comprising six Q valleys and two K valleys, as well as a normalization factor arising from the different photoemission matrix elements (between band states and photoelectron states) at the K and Q valleys (see the supplementary text, section 10). Assuming this limiting ratio reflects equilibrium at the lattice temperature of 90 K and assuming a density of state factor on the order of 1 (for details, see the supplementary materials), one can obtain a tighter bound of <0.015 eV on the energy difference of the two exciton species. A video of the exciton dynamics measured over the full BZ after resonant photoexcitation is provided in the supplementary materials (movie S1).

Finally, we turned our attention to the dynamics after above-gap excitation. We used a 2.48-eV linearly polarized pump pulse to excite carriers well above bandgap, producing an estimated carrier density of 1.6 × 10^{12}/cm^2 (see the materials and methods and supplementary text, section 16). Unexpectedly, the

exciton relaxation pathways, particularly for the dark Q-valley excitons, were substantially different from those observed for resonant excitation. Figure 4A shows snapshots of the full ARPES data at different time delays at the K and Q valleys (movie S2). Immediately after excitation (zero delay), we observed a broad distribution in the K and Q valleys centered at an energy of ~1.90 eV (fig. S11) that could involve contributions from both free carriers and excited excitonic states. Future experiments with improved time and energy resolution are needed to explore these very early dynamics (see the supplementary text, section 11). Beyond this regime, we observed full relaxation into the K- or Q-valley excitons within 500 fs (Fig. 4B). Previously, optical and mid-infrared spectroscopic measurements had reported the subpicosecond formation of exciton dynamics (*46*, *47*) but lacked separate access to the dynamics of the different types of excitonic states, such as the dark Q-valley excitons. The relaxation process can also be described by plotting the average energy of the photoemission signal versus time (Fig. 4C), giving an energy relaxation time of 500 fs. Beyond 500 fs, the peak energy of the distribution at the Q and K valleys remained constant at ~1.73 eV, matching the exciton energies under resonant conditions (Figs. 3C, inset, and 4C). A marked departure from the resonant excitation case is that Q-valley excitons appeared coincident with the K-valley excitons (rather than at a finite delay after scattering of the K-valley excitons as for the resonant excitation). We also observed that the dark Q-valley exciton density dominated the direct K-valley density at all time delays (Fig. 4C, and see inset), in contrast to the resonant excitation case. However, at long time delays, under both resonant and above-gap excitation, the system evolved to a similar quasi–steady state, with a nearly identical K-valley/Q-valley exciton population ratio and nearly degenerate exciton energies with respect to the valence band maximum. The exciton-binding energy is given by the difference between the conduction band minimum and the energy of the constituent electron photoemitted from the center of the valley at long time delays, where quasi-equilibrium is reached (*44*). Accordingly, we estimated binding energies as ~390 and ~480 meV (with respect to the conduction band minima) for the K-valley and Q-valley excitons, respectively, with a combined uncertainty of ~150 meV caused by theoretical errors, bandgap renormalization effects, and experimental uncertainty. Although the former can be compared to results of various optical spectroscopy measurements (*3*), the binding energy and momentum-space distributions of the dark exciton in monolayer TMDs are not easily accessible to other experiments (*23*).

Our measurements using TR-XUV-μ-ARPES to access strongly bound, few-particle excitonic states in 2D semiconductors and their dynamics open new possibilities. Such direct access to dark excitons or other valley- and spin-polarized excitons will enable their utility in quantum information (*48*) and valleytronic and spintronic schemes and in creating new many-body excitonic states (*9*, *10*). Energy- and momentum-resolved photoemission studies of excitons could directly image excitonic wavefunctions in momentum space. On the basis of the energy-momentum dispersion relationship, one could measure important physical properties, such as the kinetic energy and temperature of photoexcited excitons (*20*–*23*). Future measurements could access few-particle excitations, such as trions, biexcitons, and interlayer excitons in TMD heterostructures, which may be expected to have their own specific photoemission signatures. Also, the use of circularly polarized excitation would provide direct access to the nature of K to K′ exciton scattering, critical information in the context of valleytronics. Finally, we expect our measurements to extend to other condensed-matter systems in providing a complete picture of the transformation of their electronic structure along energy and momentum axes after optical illumination.

REFERENCES AND NOTES

1. P. Ajayan, P. Kim, K. Banerjee, *Phys. Today* **69**, 38–44 (2016).
2. Q. H. Wang, K. Kalantar-Zadeh, A. Kis, J. N. Coleman, M. S. Strano, *Nat. Nanotechnol.* **7**, 699–712 (2012).
3. G. Wang *et al.*, *Rev. Mod. Phys.* **90**, 021001 (2018).
4. G.-B. Liu, D. Xiao, Y. Yao, X. Xu, W. Yao, *Chem. Soc. Rev.* **44**, 2643–2663 (2015).
5. P. V. Nguyen *et al.*, *Nature* **572**, 220–223 (2019).
6. Y. Li *et al.*, *Phys. Rev. B Condens. Matter Mater. Phys.* **90**, 205422 (2014).
7. K. F. Mak, C. Lee, J. Hone, J. Shan, T. F. Heinz, *Phys. Rev. Lett.* **105**, 136805 (2010).
8. M. Cattelan, N. A. Fox, *Nanomaterials (Basel)* **8**, 284 (2018).
9. J. M. Blatt, K. W. Böer, W. Brandt, *Phys. Rev.* **126**, 1691–1692 (1962).
10. L. V. Keldysh, P. N. Lebedev, *Contemp. Phys.* **27**, 395–428 (1986).
11. M. Selig *et al.*, *Nat. Commun.* **7**, 13279 (2016).
12. A. Kormányos *et al.*, *2D Mater.* **2**, 022001 (2015).
13. J. Lindlau *et al.*, *Nat. Commun.* **9**, 2586 (2018).
14. E. Malic *et al.*, *Phys. Rev. Mater.* **2**, 014002 (2018).
15. Y. Uchiyama *et al.*, *npj 2D Mater. Appl.* **3**, 26 (2019).
16. G. Dresselhaus, *J. Phys. Chem. Solids* **1**, 14–22 (1956).
17. J. Shah, *Ultrafast Spectroscopy of Semiconductors and Semiconductor Nanostructures* (Springer, 1999)
18. H. Wang, J. Shah, T. C. Damen, L. N. Pfeiffer, *Phys. Rev. Lett.* **74**, 3065–3068 (1995).
19. E. Perfetto, D. Sangalli, A. Marini, G. Stefanucci, *Phys. Rev. B* **94**, 245303 (2016).
20. A. Steinhoff *et al.*, *Nat. Commun.* **8**, 1166 (2017).
21. A. Rustagi, A. F. Kemper, *Phys. Rev. B* **97**, 235310 (2018).
22. A. Rustagi, A. F. Kemper, *Phys. Rev. B* **99**, 125303 (2019).
23. D. Christiansen, M. Selig, E. Malic, R. Ernstorfer, A. Knorr, *Phys. Rev. B* **100**, 205401 (2019).
24. C. Poellmann *et al.*, *Nat. Mater.* **14**, 889–893 (2015).
25. A. Damascelli, *Phys. Scr.* **2004**, T109 (2004).
26. P. Hein *et al.*, *Phys. Rev. B* **94**, 205406 (2016).
27. R.-Y. Liu *et al.*, *Sci. Rep.* **7**, 15981 (2017).
28. R. Wallauer, J. Reimann, N. Armbrust, J. Güdde, U. Höfer, *Appl. Phys. Lett.* **109**, 162102 (2016).
29. R. Bertoni *et al.*, *Phys. Rev. Lett.* **117**, 277201 (2016).
30. A. Grubišić Čabo *et al.*, *Nano Lett.* **15**, 5883–5887 (2015).
31. S. Ulstrup *et al.*, *Phys. Rev. B* **95**, 041405 (2017).
32. F. Liu, M. E. Ziffer, K. R. Hansen, J. Wang, X. Zhu, *Phys. Rev. Lett.* **122**, 246803 (2019).
33. J. H. Buss *et al.*, *Rev. Sci. Instrum.* **90**, 023105 (2019).
34. M. Puppin *et al.*, *Rev. Sci. Instrum.* **90**, 023104 (2019).
35. A. K. Mills *et al.*, Cavity-enhanced high harmonic generation for XUV time-resolved ARPES. arXiv:1902.05997 [physics.optics] (15 February 2019).
36. E. J. Sie, T. Rohwer, C. Lee, N. Gedik, *Nat. Commun.* **10**, 3535 (2019).
37. A. Oelsner *et al.*, *J. Electron Spectrosc. Relat. Phenom.* **178-179**, 317–330 (2010).
38. K. Medjanik *et al.*, *Nat. Mater.* **16**, 615–621 (2017).
39. X.-X. Zhang *et al.*, *Nat. Nanotechnol.* **12**, 883–888 (2017).
40. A. Arora *et al.*, *Nanoscale* **7**, 10421–10429 (2015).
41. E. L. Wong *et al.*, *Sci. Adv.* **4**, eaat9722 (2018).
42. S. Brem, M. Selig, G. Berghaeuser, E. Malic, *Sci. Rep.* **8**, 8238 (2018).
43. M. Selig *et al.*, *2D Mater.* **5**, 035017 (2018).
44. C. Ruppert, A. Chernikov, H. M. Hill, A. F. Rigosi, T. F. Heinz, *Nano Lett.* **17**, 644–651 (2017).
45. X.-X. Zhang, Y. You, S. Y. F. Zhao, T. F. Heinz, *Phys. Rev. Lett.* **115**, 257403 (2015).
46. P. Steinleitner *et al.*, *Nano Lett.* **17**, 1455–1460 (2017).
47. F. Ceballos, Q. Cui, M. Z. Bellus, H. Zhao, *Nanoscale* **8**, 11681–11688 (2016).
48. K.-D. Park, T. Jiang, G. Clark, X. Xu, M. B. Raschke, *Nat. Nanotechnol.* **13**, 59–64 (2018).

ACKNOWLEDGMENTS

We thank the OIST engineering support section for their support. T.C. and K.M.D. thank F. H. da Jordana for discussions. J.M., M.K.L.M., and K.M.D. thank D. Bacon for experimental support. **Funding:** This work was supported by JSPS KAKENHI grant no. JP17K04995 and by the Femtosecond Spectroscopy Unit, Okinawa Institute of Science and Technology Graduate University. Theoretical analysis and first-principle calculations were partially supported by the National Science Foundation (NSF) through the University of Washington Materials Research Science and Engineering Center DMR-1719797. Analysis at SLAC was supported by the AMOS program, Chemical Sciences, Geosciences, and Biosciences Division, Basic Energy Sciences, U.S. Department of Energy under contract no. DE-AC02-76-SF00515. T.C. acknowledges support from the Micron Foundation and a GLAM postdoctoral fellowship at Stanford. Computational resources were provided by Hyak at the University of Washington and the Extreme Science and Engineering Discovery Environment (XSEDE), which is supported by the NSF under grant no. ACI-1053575. The work of M.C. and X.L. at University of Texas at Austin was partially supported by the NSF through the Center for Dynamics and Control of Materials (NSF MRSEC under cooperative agreement no. DMR-1720595) and the facility supported by the center. **Author contributions:** J.M., M.K.L.M., and K.M.D. designed the experimental setup. J.M., M.K.L.M., and C.S. built the experimental setup. J.M., M.K.L.M., C.S., E.L.W., and A.A.M. performed the experiments. J.M., M.K.L.M., A.A.M., and N.S.C. analyzed the data. J.M., C.S., E.L.W., and B.M.K.M. designed and built the XUV source. V.P. and A.K. characterized the sample. M.C. and X.L. prepared the sample. T.F.H. and T.C. provided theoretical support. T.C. performed first-principle theoretical calculations. K.M.D. supervised the project. All authors contributed to discussions and manuscript preparation. **Competing interests:** J.M., M.K.L.M., and K.M.D. are inventors on a patent application related to this work filed by the Okinawa Institute of Science and Technology School Corporation (US 2020/0333559 A1 published on October 22, 2020). The authors declare no other competing interests. **Data and materials availability:** All data are available in the manuscript or supplementary materials.

SUPPLEMENTARY MATERIALS

science.sciencemag.org/content/370/6521/1199/suppl/DC1
Materials and Methods
Figs. S1 to S14
References (*49*–*60*)
Movies S1 and S2

20 April 2020; accepted 29 September 2020
10.1126/science.aba1029

Directly visualizing the momentum-forbidden dark excitons and their dynamics in atomically thin semiconductors

Julien Madéo, Michael K. L. Man, Chakradhar Sahoo, Marshall Campbell, Vivek Pareek, E. Laine Wong, Abdullah Al-Mahboob, Nicholas S. Chan, Arka Karmakar, Bala Murali Krishna Mariserla, Xiaoqin Li, Tony F. Heinz, Ting Cao and Keshav M. Dani

Science **370** (6521), 1199-1204.
DOI: 10.1126/science.aba1029

Probing the dark state

Excitons, electron-hole pairs held together by Coulomb attraction, can be generated in semiconductors under excitation and greatly influence the material's optoelectronic properties. Although bright excitons are optically active, their dark-state cousins have been more difficult to detect. They do, however, affect the optoelectronic properties through their interaction with light and bright excitons. Madéo *et al.* developed a pump-probe photoemission technique that is used reveal the spatial, temporal, and spectral dynamics of excitons (see the Perspective by Na and Ye). Demonstrated in two-dimensional monolayer films of tungsten diselenide, the technique could also be applicable to other semiconductor systems hosting excitonic excitations.

Science, this issue p. 1199; see also p. 1166